Physica B 731 (2026) 418513

Contents lists available at ScienceDirect

Physica B: Condensed Matter

journal homepage: www.elsevier.com/locate/physb

Controlling magnon propagation and frequency gap through the fan angle of a sinusoidal bias field

P. Micaletti, A. Visonà, F. Montoncello *

Dipartimento di Fisica e Scienze della Terra, Università degli Studi di Ferrara, Ferrara, Italy

ARTICLE INFO

Keywords:
Magnons
Spin waves
Ferromagnetic resonance
Micromagnetic simulations
Green computing

ABSTRACT

We investigate through micromagnetic simulations the spin-dynamics of a ferromagnetic film to which a sinusoidal magnetic field is applied with fixed magnitude and variable fan angle Θ_F. At equilibrium, the magnetization relaxes in a likewise sinusoidal distribution with an amplitude depending on Θ_F. We illustrate in detail how the dispersion curves and the frequency gap at zone boundary vary with Θ_F, discussing the functional behavior and the correlation to the potential energy density. We also discuss the extent and limits to which the Kittel formula can be used in computing the resonance frequencies even for sinusoidal magnetizations, definitely far from being uniform. In conclusion, we demonstrate that it is possible to achieve full control on magnon propagation through Θ_F as a sole degree of freedom. This allows to keep the field magnitude constant and small, reducing energy dissipation at a minimum, with positive implications for dissipationless magnon-devices.

1. Introduction

3D Magnonics [1] explores the manipulation and propagation of spin waves in 3D nanostructures, enabling an advanced control of the information transfer at the nanoscale, for applications in magnon-spintronic devices [2] and next-generation computing technologies [3–6]. A magnetic film layer generally maintains a uniform magnetic distribution unless it is physically corrugated [7–11] or coupled with a patterned overlayer [12]. Such a pattern might be irregular though produced by a deterministic rules, like Fibonacci or Penrose tiling structures [13–16], or regular and periodic, like artificial spin ice systems [17–22], periodic ferroelectric domain polarization in multiferroics [23,24], and even periodic superconducting structures [25–27]. The presence of a non-uniform magnetization in a ferromagnetic film produces confinement effects typical of patterned structures, in particular numerous spin wave modes, which provide additional degrees of freedom, with respect to the single one of the uniform film, extremely useful for signal manipulation. In the investigation carried out in Ref. [28], we studied the evolution of magnonic band structures in a ferromagnetic film when a sinusoidal field is applied with variable amplitude. In the experiments, this field can be directly applied to the system by means of an electromagnetic coil (solenoid), with a given pitch (determining the space period, i.e., lattice constant), through which a current flows, with an intensity which determines both the magnitude of the sinusoidal field, and the fan angle of the magnetization undulation (see Appendix for a detailed description, and Refs. [29,30] for previous experimental partial attempts). In the context of a multilayer geometry, the sinusoidal field can be produced by the vertical coupling with an overlayer with a periodic pattern (ferromagnetic, ferroelectric, superconducting and so on) [23]. Hence, the sinusoidal field we used is ultimately the simulation of any of the above periodic mechanisms. In the same study we focused on the effect on the magnonic band structure of an increasing magnitude of such a sinusoidal field. Here, instead, we study the influence of its fan angle (i.e., its angular spread) at a fixed magnitude. It is not trivial to identify a good degree of freedom to manipulate the spin wave dynamics (group velocity, frequency gap, effective mass etc.) without the help of any magnetic field or electric current variations. We demonstrate that varying the fan angle (hence, geometry) at a fixed (and possibly small) magnetic field magnitude can produce the same results that strong field magnitude variations would produce, with important consequences in the mitigation of the Joule effect [31,32]. The experimental realization of this geometric variation might be challenging, nevertheless we suggest a few possibilities, keeping in mind that our very purpose is to present a potential scenario, indicating a path for further experimental investigations. Our simulations also find that, as a function of the fan angle, the frequency gap follows a quadratic functional behavior, which we correlate to the behavior of the total energy density, and, in turn, to the behavior of the total magnetic field.

* Corresponding author.
E-mail address: montoncello@fe.infn.it (F. Montoncello).

https://doi.org/10.1016/j.physb.2026.418513
Received 9 February 2026; Received in revised form 27 February 2026; Accepted 10 March 2026
Available online 11 March 2026

We observe that our approach, based on the implementation of a sinusoidal spin pattern, could be easily extended to the case of a fan angle equal to 2π, namely to spin cycloid structures [33,34]: these special spin textures could be also obtained through appropriate ferroelectric domain distributions and can give origin to non-reciprocal effects which are outside the scope of the present investigation.

Compared to other magnonic crystals, the one we present is continuous, in contrast to the discontinuous ferromagnetic dot/antidot arrays [35–40], and made of a single material, in contrast to films with periodically modulated magnetic properties [41–43], and hence possesses a inherent simplicity, which transfers also to the dynamics. At the same time, it can be controlled in real-time, i.e., without changing the system itself, by tuning some external parameter (e.g., the fan angle, subject of our investigation): this property is considered extremely valuable and the corresponding systems are called *dynamic* magnonic crystals [29,44,45], since the magnon properties (frequency gap width and position, group velocity, effective mass, wave packet dispersion, etc.) can be tuned *during* their propagation. In addition, we address the issue of waste heat and low-dissipation technologies.

2. Methodology

We perform micromagnetic simulations by means of the GPU-accelerated software MuMax3 [46]. In order to simulate an extended, realistic square system, quasi-periodic boundary conditions [47] are applied, with 800 copies of the primitive cell along each coordinate axis. We apply a uniform bias field $B_0 = 0.1$ T parallel to the x direction, just to obtain, as a reference, a FMR frequency around 10 GHz when the film is uniformly magnetized.

Furthermore, as the key item of the present investigations, we add a non-uniform, sinusoidal magnetic field $\boldsymbol{B_S}$, and consider either its magnitude (B_S) or fan angle (Θ_F) variation. B_S varies from 0 to 0.1 T with steps of 0.01 T, Θ_F varies from 0 to π with steps of $\pi/6$. As shown in Fig. 1, Θ_F depends on the undulation amplitude of the field, which can be written as:

$$Y_0 = \frac{B^0_{Sy}}{B^0_{Sx}} \frac{a}{2\pi}, \tag{1}$$

where a is spatial period of the oscillation (lattice constant), and $B^0_{Sx,y}$ are the x and y components of the sinusoidal field taken at the origin ($x = 0$). Being x the oscillation direction, we consider two polarization planes for B_S: xy (in-plane polarization) and xz (out-of-plane polarization): after the application of B_S, the film magnetization relaxes at equilibrium to a sinusoidal distribution, the amplitude of which depends (for a given B_0) on both B_S and Θ_F.

We consider a 5-nm-thick magnetic film layer made of permalloy, with the following magnetic parameters: saturation magnetization $M_S = 800$ kA/m, exchange stiffness $A_{ex} = 10$ pJ/m, and gyromagnetic ratio $\gamma = 185$ rad GHz/T. The primitive cell of the system (Fig. 1, panel (a)) is a square with side $a = 256$ nm (lattice constant) and thickness 5 nm. The system is discretized into micromagnetic cells with dimension $4 \times 4 \times 5$ nm^3.

In order to calculate the dispersion curves by means of Fourier analysis, we replicate the primitive cell 200 times along the x-axis, creating a supercell of dimensions $51200 \times 256 \times 5$ nm^3. This allows a wavevector resolution of $0.122 \cdot 10^{-3}$ rad/nm.

To the relaxed magnetization (a stable equilibrium configuration), we apply a non-uniform sinc microwave field for 100 ns and save the time resolved magnetization maps at intervals of $dt = 25$ ps. This allows a frequency resolution of 0.01 GHz and a maximum frequency of 20 GHz. On those magnetization maps, we perform a space–time Fast Fourier Transform to get the dispersion relations. Additional details regarding the sinc and the simulations can be found in Ref. [28].

Furthermore, we will compare the film with a sinusoidal magnetization to an effective film with a uniform magnetization: to that purpose, we focus on the equivalence between the relaxed magnetization under

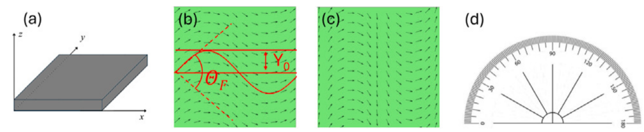

Fig. 1. Panel (a): adopted reference system. Sketches of B_S vector field distributions when (b) $\Theta_F = \pi/2$ and (c) $\Theta_F = \pi$. In panel (b) the fan angle and the undulation amplitude Y_0 are explicitly indicated. The undulation amplitude in (c) is larger than in (b) (the green color marks the background, the arrows are only illustrative of the undulation). Panel (d): fan angles considered throughout the investigation.

$\boldsymbol{B} \equiv \boldsymbol{B_S} + \boldsymbol{B_0}$ and the relaxed magnetization under a uniform field applied to the system. In particular, we aim to determine the value B^* of the uniform field that, applied alone to an uniformly magnetized film, would give the same energy density of the simulated system with a sinusoidal magnetization subject to the magnetic field $\boldsymbol{B}$ (equivalence).

Therefore, we make use of the Kittel formula for a thin film [48]:

$$\omega = \gamma \sqrt{B^*(B^* + \mu_0 M_S)}, \tag{2}$$

where γ is the gyromagnetic ratio, B^* is the uniform field applied to the system, μ_0 the magnetic permeability of the vacuum, and M_S the saturation magnetization.

The *magnetic energy density* is given by:

$$u = -\sum_i (M^i_x B^i_x + M^i_y B^i_y + M^i_z B^i_z), \tag{3}$$

where the summation index goes over all the micromagnetic cells in the primitive cell, the magnetization components M_x, M_y, M_z are obtained after the relaxation process and the magnetic field components B_x, B_y, B_z represent the contributions of B_S and B_0. Clearly, the better the discretization of the micromagnetic cell, the more accurate the computed energy density: this aspect will be addressed in Section 3 and represents an important validation of the simulations. The energy density can also be expressed in terms of the saturation magnetization M_S as follows:

$$u = -M_s B^*. \tag{4}$$

In this approach, B^* reproduces in the uniform film what B does in the sinusoidally magnetized one to provide the same energy density, within a certain accuracy. By requiring the equivalence between the energy densities of Eqs. (3) and (4), we obtain a fictitious field B^*, which should enter the Kittel formula (Eq. (2)) to provide the exact resonance frequency found by the micromagnetic simulations, for each value of B_S or Θ_F.

3. Results

The application of $\boldsymbol{B_S}$ makes the film magnetization relax into a sinusoidal distribution, with a spatial amplitude correlated to the sinusoidal field magnitude B_S and fan angle Θ_F, if a fixed B_0 is considered (in the following, 0.1 T). As an example, in Fig. 3 we show the equilibrium magnetization when the sinusoidal field $\Theta_F = \pi/2$ (panel (a)), and when $\Theta_F = \pi$ (panel (b)): visibly, in the second case the undulation amplitude of the magnetization is larger.

Being in our case the oscillation only along a single direction (x-axis), the induced periodicity turns the film into a one-dimensional (1-D) magnonic crystal. Therefore, along that direction, magnons undergo Bragg's diffraction and their dispersion curve shows the distinctive marks: *periodic folding* to the reduced Brillouin zone and *frequency gaps* at the Brillouin zone boundary. In Ref. [28] we observed that in undulated systems the actual (physical) lattice constant d governing the spin-wave dynamics is a half of the geometric one, i.e., $d = a/2$. Hence, the actual first Brillouin zone boundary occurs at $k = 0.0245$ rad/nm,

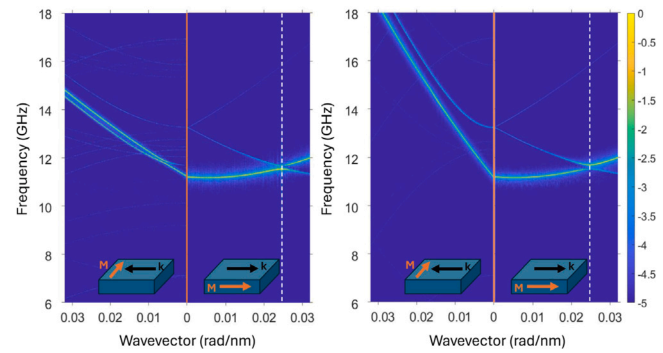

Fig. 2. Band structure for a sinusoidal magnetization polarized in-plane (left panel) and out-of-plane (right panel), when B_S = 0.03 T. On the left half of each panel the DE dispersions are plotted, while on the right half of each panel the BV dispersions are plotted. The dashed white line marks the zone boundary (k = 0.0245 rad/nm), where a frequency gap opens. The color bar on the right represents intensity in arbitrary units.

i.e., twice the geometric one (0.01225 rad/nm). The underlying reason is that the spin-wave spectrum is invariant under a horizontal mirror operation σ_y on the magnetization, and that corresponds to a sign inversion of its y component. This additional symmetry is responsible for the doubling of the actual Brillouin zone boundary.

The application of a bias field that is periodic along a direction (x-axis) influences the dynamics also in the transverse direction (y-axis), since new modes arise as Bloch waves, additional to the film spin-wave. In our case, since the magnetization vector flux is oriented parallel to the x-direction, the backward volume (BV) mode dispersion shows the typical band structure, and the folding to the reduced Brillouin zone determines new modes at $k = 0$ which were not present in the uniformly magnetized film. These modes have a cell function with a progressively increasing number n of backward nodes, i.e., nodal lines perpendicular to the magnetization direction: n-BV. Hence, these new modes, generated by the folding of the BV dispersion, are the cell function of new Bloch waves which can propagate also along y as Damon–Eshbach (DE) waves, and produce their individual dispersion. In Fig. 2 we show the band structure for sinusoidal magnetized films with $B_S = 0.03$ T ($\Theta_F = \pi$) in the two undulation polarizations xy (left panel) and xz (right panel). The right half of each panel shows the band structure of BV modes (characterized by periodicity), while the left half shows the DE dispersions of the first two modes, specifically the fundamental one, also named 0-BV, and the 1-BV. In fact, the higher order modes are not perceptible in the plots. Hence, even if periodicity is not present along this direction, the dynamics is influenced as well.

3.1. Fan angle as a degree of freedom: mechanism and advantages

Now we investigate the role of Θ_F in controlling the equilibrium magnetization and hence both the magnon band structure and frequency gap. As observed in Section 1, a sinusoidal magnetization can be induced in a film in many ways. Hence, in real experiments, Θ_F can be changed depending on the specific used method. For example, Θ_F can be varied by varying the polarization direction of each ferroelectric domain, if a ferroelectric/ferromagnetic heterojunction is concerned [49,50], or by varying the meander-type geometry, if a current flow is used (see Appendix and Ref. [29]) and so on.

In the next simulations, we fix $B_S = 0.07$ T and vary Θ_F.

Clearly, both Θ_F and B_S magnitude concur to produce similar effects on the magnetization undulation: in particular, different combinations of B_S and Θ_F can produce precisely the same magnetization undulation. This is an interesting result, overlooked until now, particularly useful when aiming to reduce the applied field magnitude, e.g., to

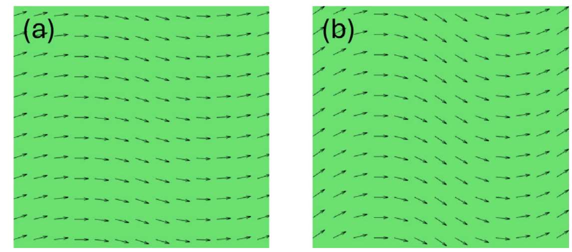

Fig. 3. Magnetization distribution after relaxation to sinusoidal fields with $B_S = 0.1$ T and $\Theta_F = \pi/2$ (a) or $\Theta_F = \pi$ (b) (the sinusoidal fields are shown in Fig. 1 in panels (a) and (b)). Higher fan angles result in a larger undulation amplitude. The presence of the additional uniform field $B_0 = 0.1$ T justifies the mismatch between B_S and magnetization profiles.

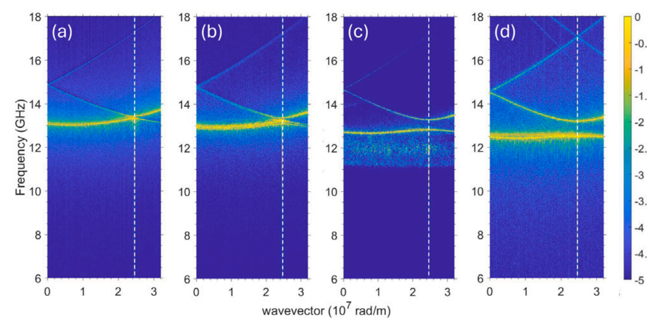

Fig. 4. Magnonic band structures for BV waves (B_0 = 0.1 T, B_S = 0.07 T, polarization in the xy plane) and different Θ_F. Panel (a): $\Theta_F = \pi/3$. Panel (b): $\Theta_F = \pi/2$. Panel (c): $\Theta_F = 5\pi/6$. Panel (d): $\Theta_F = \pi$. Zone boundary occurs at $k = 0.0245$ rad/nm, marked by the dashed white line. The color bar on the right represents intensity in arbitrary units.

contain power dissipation: playing with the fan angle only at a fixed, low B_S is effective to the purpose.

To prove this, in Fig. 4 we plot the BV dispersion curves at four different values of Θ_F. A first effect is that increasing Θ_F (while B_S is fixed) determined a general frequency downshift. The explanation of this behavior is twofold: from one side, the progressively increasing magnetization amplitude makes the angle between the total bias field $\boldsymbol{B}_S(x,y) + \boldsymbol{B}_0$ and the magnetization $\boldsymbol{M}(x,y)$ larger at any given point (x,y). This reduces the Zeeman potential energy (which depends on the scalar product) and hence the mode frequency. From the other, the progressive increase of the undulation amplitude increases the divergence of the magnetization and hence makes the internal dipolar fields larger, which follows in a general decrease of the internal effective field and hence of the mode frequency [51].

The second remarkable effect is that the frequency gap at zone boundary increases for increasing Θ_F. In Ref. [28] we explained the presence of such a gap in terms of the interaction between B_S and the magnon profiles. More precisely, the spin-wavefunctions of the fundamental mode (FM, also called 0-BV) and 1-BV, which at zone boundary are indistinguishable after a translation of half a primitive cell, and hence in principle degenerate, are no longer degenerate in frequency because of their different phase relationship with B_S oscillation. Then, the two waves do experience B_S in different ways with different outcomes: the former achieving the lowest frequency (the top of the lower band), the latter the highest frequency (the bottom of the upper band), hence producing a visible frequency gap. Since we already established that increasing Θ_F at a fixed B_S produces an increased undulation amplitude in the magnetization, the effect is equivalent of increasing B_S at a fixed Θ_F: hence, by increasing Θ_F the frequency difference (gap) between the two modes increases.

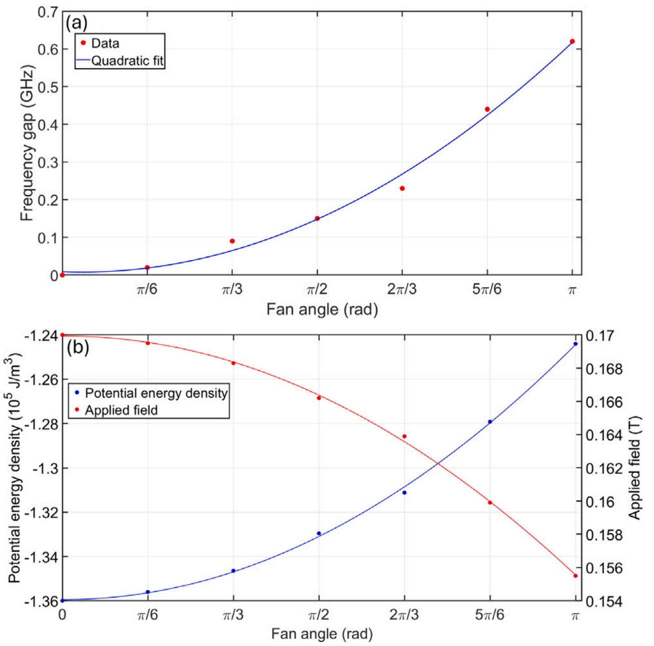

Fig. 5. Panel (a): frequency gap as a function of Θ_F for $B_S = 0.07$ T (magnetization in xy plane). Red dots: micromagnetic simulations. Blue line: best fit, which is quadratic to a first approximation. Referring to Eq. (5), $a = 0.0669$, $b = -0.0164$, $c = 0.0088$. Panel (b): potential energy density u (blue dots) with the corresponding quadratic fit (blue line) and applied field $\boldsymbol{B}$ (red dots) with the corresponding quadratic fit (red line).

This is shown in Fig. 5, Panel (a), where the frequency gap values (red dots) are plotted together with the calculated specific trend (blue line). In particular, to a first approximation, the best fit turns out to be quadratic, i.e., with a functional behavior of the form:

$$y(x) = ax^2 + bx + c, \tag{5}$$

being y the frequency gap, x the fan angle, and a, b, c appropriate coefficients. The system exhibits an equilibrium configuration where the potential energy as a function of the fan angle, $u(\Theta_F)$, assumes a *parabolic* expression (Fig. 5, Panel (b), blue line). This trend shifts to the magnon frequencies, and in turn to the gap. Considering Eq. (2), a parabolic energy density is produced by a likewise parabolic behavior of the applied field magnitude (Fig. 5, Panel (b), red line), which, substituted in the Kittel formula, determines a parabolic behavior in frequency (Fig. 6). We remark that this result, despite apparently simple, was overlooked until now, so here we aim to add this piece of information, considering its importance in the context of searching new degrees of freedom for magnon manipulation at the nanoscale.

We checked that this parabolic behavior is observed, independently of the specific value of B_0, until a critical fan angle Θ_F^{crit} is reached. Considering variations of the uniform field magnitude B_0, when $B_0 > B_S$, we find that $\Theta_F^{\text{crit}} = \pi$, covering a full angular excursion of the applied magnetic vector field. When instead $B_0 \leq B_S$, then $\Theta_F^{\text{crit}} \approx 2\pi/3$, covering a limited angular excursion. Hence, Θ_F^{crit} depends primarily on the relative strength B_0/B_S, where B_S tends to increase the undulation amplitude and fan angle of the magnetization, while B_0 opposes to it, tending to stretch the magnetization toward uniformity. When this ratio is too small, large fan angles of B_S would cause large magnetization fan angles as well. This strong perturbation of the ground state magnetization, in turn, would involve powers larger than 2 in Eq. (5).

In conclusion, by operating on Θ_F at a fixed B_S it is possible to tune the width of the frequency gap and the frequency region where it is located. Hence the gap can be easily varied even if B_S is kept constant and possibly low, to minimize the waste heat.

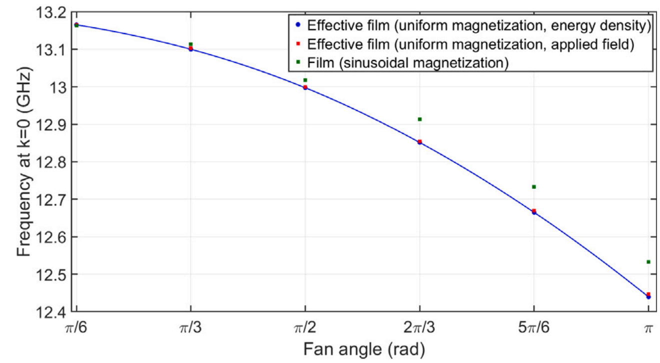

Fig. 6. Frequency calculated at $k = 0$ as a function of Θ_F (magnetization in xy plane) for $B_S = 0.07$ T. Green dots: film with a sinusoidal magnetization (simulations). Red dots: effective film with a uniform magnetization subject to exactly the same $\boldsymbol{B}$ used in the simulations. Blue dots: effective film with a uniform magnetization subject to a B^* which gives the potential energy density of the simulation (the line is a guide for the eye).

3.2. FMR for undulated magnetizations and Kittel formula

The Kittel formula is normally used to calculate the ferromagnetic resonance (FMR) of uniformly magnetized films, and its simplicity makes it very popular to get dynamic information on ferromagnetic samples. We wonder to what extent the formula can be used to deal with undulated magnetizations, quantifying the approximations: this investigation will help us understand more in depth the role of the fan angle in controlling the magnetization dynamics.

Our purpose is to compare two systems: from one side, the film with undulated magnetization subject to both a uniform bias field B_0 (fixed to 0.1 T) and a sinusoidal bias field B_S, the results of which were found through micromagnetic simulations. From the other, a fictitious uniformly magnetized film, to which we apply the same field magnitude of the previous system, i.e., the same magnitude of $\boldsymbol{B} = \boldsymbol{B}_0 + \boldsymbol{B}_S$ (the vector summation takes into account the local orientation of $\boldsymbol{B}_S$). We wonder under what conditions the two systems give the same resonance frequencies at zero wavevector.

As a first step to that purpose, for each fan angle Θ_F we compare the resonance frequencies found in the simulations (i.e., for a sinusoidal magnetization under $\boldsymbol{B} = \boldsymbol{B}_0 + \boldsymbol{B}_S$) with the resonance frequencies of an effective uniformly magnetized film, calculated with the Kittel formula using a uniform field determined with two different approaches: in one case we utilize the same $\boldsymbol{B}$ of the simulation forcing it to be uniform by means of the following equation:

$$|\boldsymbol{B}| = \frac{\sum_i^N \sqrt{(B_x^i)^2 + (B_y^i)^2}}{N}, \tag{6}$$

where the value of $\boldsymbol{B}$ is computed as the average over the entire primitive cell. In the other case, we use an effective field, which gives the same potential energy density u of the simulations.

The comparison, for the three cases, is plotted in Fig. 6. In this figure we see three points per angle: first, the results of the simulations (sinusoidal magnetization, green squares), then the results of the Kittel formula using the same magnetic field (red circles), and finally the results of the Kittel formula using the same potential energy density (blue circles, with the blue line as guide for the eye). When Θ_F is increased, the resonance frequencies decrease, for the reasons explained in Section 3.1.

While the frequencies of the effective film calculated by means of the Kittel formula in either methods are almost identical, they are systematically lower than the frequencies found with simulations and related to the sinusoidal magnetization. The mismatch between the frequencies of the effective uniform film and those of the undulated

Table 1
Comparison of $\boldsymbol{B}$, determined according to Eq. (6) and B^* calculated with the Kittel formula (for an effective uniform film), and B^* calculated with micromagnetic simulations (film with sinusoidal magnetization) for $B_0 = 0.1$ T and $B_S = 0.07$ T (polarization along the xy plane).

	Θ_F (rad)					
	$\pi/6$	$\pi/3$	$\pi/2$	$2\pi/3$	$5\pi/6$	π
$\boldsymbol{B}\vert B^*$ uniform (T)	0.1695	0.1681	0.1658	0.1625	0.1584	0.1534
B^* sinusoidal (T)	0.1695	0.1683	0.1662	0.1639	0.1599	0.1555

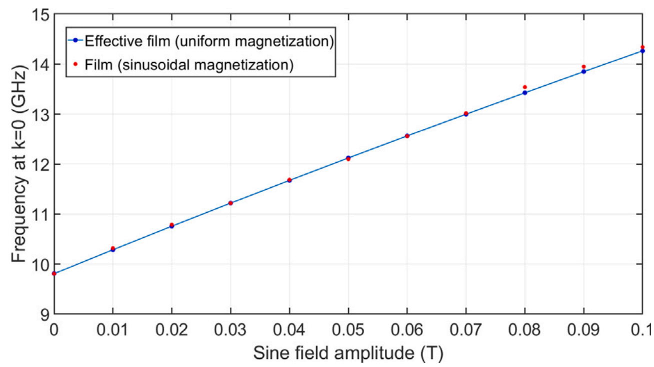

Fig. 7. Resonance frequencies as a function of B_S after imposing the equivalence of the energy density (magnetization undulation in xy plane). Red dots: simulations on a film with sinusoidal magnetization. Blue dots: uniformly magnetized film. The slight discrepancy at high amplitudes is due to the micromagnetic grid resolution.

film becomes larger for increasing Θ_F, showing the limits of the approximation through the effective uniformly magnetized film. At the same time, it helps in quantifying the approximation error to a maximum of 0.8%, which might be acceptable under some conditions.

The same concept can be extracted from Table 1, where the magnetic fields necessary to give the same resonance frequency are calculated at different Θ_F values (and fixed field magnitude $B_S = 0.07$ T). Remarkably, the Kittel formula is in good agreement with simulations up to rather large angles (e.g., $\pi/2$), where a mismatch becomes appreciable only on the third significant digit. Of course, the Kittel formula is ineffective in accounting for very large amplitude magnetization undulations.

The second step is to compare the frequencies of the two systems after imposing the equivalence of the energy density while either the fan angle or the magnitude of B_S is increased.

To this purpose, as explained in Section 2, we first calculate the fictitious uniform field B^*, which would give the same energy density of the sinusoidal one, and then insert it in the Kittel formula to obtain the corresponding ferromagnetic resonance frequency. In Fig. 7 we compare the resonance frequencies obtained with this method with the results of the simulations on the actual sinusoidal magnetization.

The agreement is very good, which confirms the leading role of the energy density in determining the ultimate magnon frequencies. The slight mismatch at $B_S \geq 0.08$ T is due again to the micromagnetic discretization resolution.

To confirm that the discrepancy is only due to the micromagnetic discretization, we use smaller micromagnetic cells in a couple of dedicated simulations. We consider a half of the previous micromagnetic cell size, i.e., $2 \times 2 \times 5$ nm^3 and then a quarter, i.e., $1 \times 1 \times 5$ nm^3, while the physical system is left unchanged. We find that the corresponding frequencies get closer to the ones calculated with the Kittel formula: as an example, for an applied $B_S = 0.09$ T, the frequency found in the simulations is 13.95 GHz for a $4 \times 4 \times 5$ nm^3 micromagnetic cell, 13.88 GHz for a $2 \times 2 \times 5$ nm^3 micromagnetic cell, and 13.85 GHz for a $1 \times 1 \times 5$ nm^3 micromagnetic cell. The last value coincides with

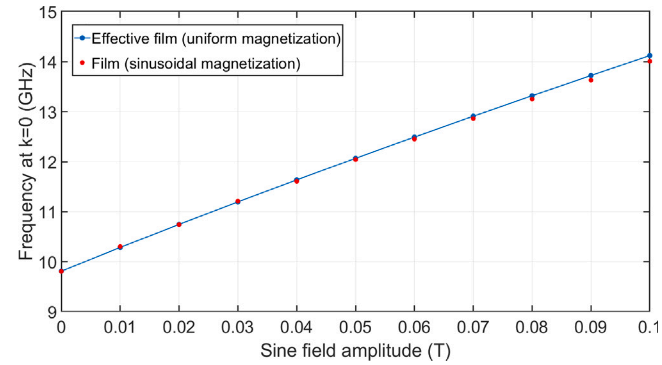

Fig. 8. Resonance frequencies as a function of B_S (magnetization in xz plane). Blue dots: frequencies of the uniformly magnetized film after imposing the equivalence of the energy density (the line is a guide for the eye). Red dots: simulations on the sinusoidal magnetization.

the one derived with the Kittel formula (13.85 GHz, Fig. 7), showing that a very refined discretization improves the agreement. However, the corresponding computational effort in terms of memory and time would be almost impracticable.

The agreement of this approach (equivalence of the energy density) and the simulations is very good also when the magnetization is in the xz plane (see Fig. 8).

A little mismatch occurs only for $B_S \geq 0.08\ T$, where the analytical approach provides frequencies slightly larger than those found in the corresponding simulations: again, this is due to computational artifacts. In fact, since the magnetization lies in the xz plane and only a single micromagnetic layer is present (film thickness equal to the micromagnetic cell thickness), in this case the dipolar fields are always antiparallel to the magnetic moments, favoring a (slight) frequency decrease (computational artifact). This is in contrast to the previous case, where the magnetization lied in the xy plane: with reference to any given magnetic moment, there were also neighboring magnetic moments almost parallel (head-to-tail direction), a condition which favors magnetization stability (stiffness) and hence a frequency increase. In conclusion, even in the xz-plane configuration we recognize the energy density as the ruling ultimate parameter for the spin dynamics, and the Kittel formula a still valid tool for getting the resonance frequencies in films with sinusoidal magnetization.

4. Conclusions

We investigated the behavior of a ferromagnetic film under the influence of a sinusoidal magnetic field with variable fan angle Θ_F. We demonstrated that it is possible to control the magnon dynamics in a ferromagnetic film by varying only the fan angle of an applied sinusoidal field, while its magnitude is left unchanged. The importance of this finding is that it allows to keep the magnetic field magnitude very small, considerably limiting the waste heat, and though maintain a full control over the magnon dynamics through the fan angle only.

In particular, we found that the frequency gap increases with increasing Θ_F in a quadratic functional behavior, while its overall position shifts towards lower frequencies. The trend is quadratic until a critical angle Θ_F^{crit} which is π when $B_0 > B_S$, and reduces to $2\pi/3$ when $B_0 \leq B_S$. We provided also the physical interpretation of the quadratic behavior, as the result of a similar behavior of the total applied field and total energy density found both in the simulations and in an analytical model based on the Kittel formula.

In fact, we found that, despite nonuniform, such a special distribution of the magnetization still allows the use of the Kittel formula to obtain the FMR frequencies at any B_S fan angle or magnitude. We investigated to what extent and precision this is possible.

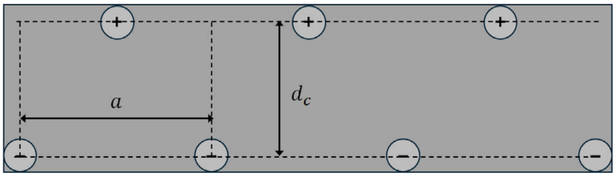

Fig. 9. Sketch of the cross section of the system: circles represent the intersections of the electromagnetic coil with the film plane, while the signs "+" and "-" indicate the current flow direction with respect to the film plane. "a" is the lattice constant (period) and d_c the coil diameter.

In conclusion, as a prospect, we observe that, in the context of ferroelectric/ferromagnetic (FE/FM) bilayers, the application of a sinusoidal *electric field* with variable fan angle to the FE layer could represent a challenging progress of the system we have studied. Indeed, through inverse magnetostriction, the sinusoidal electric field would generate in the FM layer a sinusoidal internal magnetic field (which we generated through B_S), and, as a consequence, the fan angle of an electric field would be the sole degree of freedom to get full control of the magnon dynamics in the FM layer, without the presence of any magnetic field. For this reason, we believe that our investigation represents an interesting step forward in the research toward extremely low-dissipation magnonic devices for information transfer and manipulation.

CRediT authorship contribution statement

P. Micaletti: Writing – review & editing, Writing – original draft, Investigation. **A. Visonà:** Investigation, Writing – review & editing. **F. Montoncello:** Writing – review & editing, Writing – original draft, Supervision, Software, Project administration, Methodology, Investigation, Funding acquisition, Formal analysis, Data curation, Conceptualization.

Declaration of competing interest

The authors declare that they have no known competing financial interests or personal relationships that could have appeared to influence the work reported in this paper.

Acknowledgments

Authors acknowledge support by the Department of Physics and Earth Sciences-University of Ferrara Grant Bando FIRD 2024, as well as the CINECA award under the ISCRA initiative, for the availability of high performance computing resources and support.

Appendix. A sinusoidal magnetic field resulting from a current-carrying electromagnetic coil

While a discrete domain distribution of magnetic anisotropy was proven to provide an exact sinusoidal field in Ref. [23], in this Appendix we provde details on how to reproduce, in practice, a sinusoidal magnetic field (B_S) by means of an electric current i flowing through a conducting coil (solenoid).

The scheme we adopt is shown in Fig. 9, where the cross section of the ferromagnetic film, crossed by the conducting coil, is sketched limited to three primitive cells. We used the periodic boundary conditions to simulate an infinite system. The current flow direction, with respect to the film plane, is indicated by the signs "+" (outside) and "-" (inside).

The simulations are based on the laws of classical electrodynamics, in particular the Ampère's law (magnetic field circulation vs. current intensity):

$$\oint \mathbf{B} \cdot d\mathbf{s} = \mu_0 i, \tag{7}$$

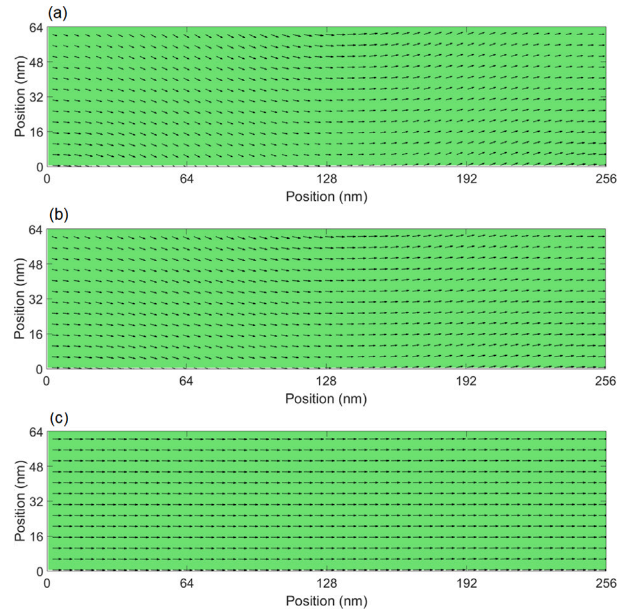

Fig. 10. Magnetic field vector maps (limited to two periods) generated by a current-carrying coil with (a) d_c = 168 nm, which determines $\Theta_F \approx 47°$; (b) d_c = 248 nm, determining $\Theta_F \approx 33°$; (c) in this case still d_c = 168 nm, but we added a uniform B_0 = 0.04 T which determines $\Theta_F \approx 2.7°$. (b) and (c) show the *stretching effect* operated through two different control parameters.

and the consequent Biot–Savart law, providing the magnetic field generated by current i:

$$\mathbf{B}_j = \frac{\mu_0}{2\pi} \frac{i}{|r - r_{0j}|} \hat{\mathbf{z}} \times \hat{\mathbf{r}}, \tag{8}$$

where $\hat{\mathbf{z}}$ is the unit vector normal to the film plane, $\mathbf{r}$ is the position vector, $\mathbf{r}_{0j}$ is the position vector of the jth wire (with $|r - r_{0j}|$ larger than the wire radius), $\hat{\mathbf{r}}$ is the corresponding unit vector, μ_0 is the magnetic permittivity in vacuum. Then, since the coil intersects the ferromagnetic film in several points, each generating its own magnetic field (with alternating circulations), we use the principle of superposition of fields:

$$\mathbf{B}_S = \sum_{j=1}^{N} \mathbf{B}_j, \tag{9}$$

where N is the number of contact crossings the coil does through the film (i.e., the coil has $N/2$ turns).

The resulting vector field (far from the line of the coil contacts) tends to a sinusoidal distribution, with a spatial amplitude and fan angle (see Fig. 1), which primarily depend on the distance d_c between the "+" and "−" rows (diameter of the coil). Hence, in practice the fan angle can be intrinsically tuned by varying d_c through (e.g.) a piezoelectric device. However, following the discussion at the end of Section 3.1, also a small uniform bias field B_0 can help to the purpose, since it contrasts the effects of B_S.

In order to show how the two different parameters change the fan angle, we plot in Fig. 10 three vector maps of the total magnetic field. The simulations were performed applying a current density $J = 5.0 \cdot 10^{11}$ A/m^2 (see Refs. [52,53]) for a conducting wire section of radius 20 nm (hence, i = 0.628 mA). The solenoid pitch matches the lattice constant (a = 256 nm). The value of J determines the magnitude of B_S, and, hence, is crucial to understand in which range B_0 must lie to compete with B_S. In the same Fig. 10, first we plot the reference map where the contact distance is d_c = 168 nm and the uniform bias field is $B_0 = 0$, for which we calculated a $\Theta_F \approx 47°$. Then, we plot the case where d_c = 248 nm, i.e., is increased of 80 nm: in this case $\Theta_F \approx 33°$.

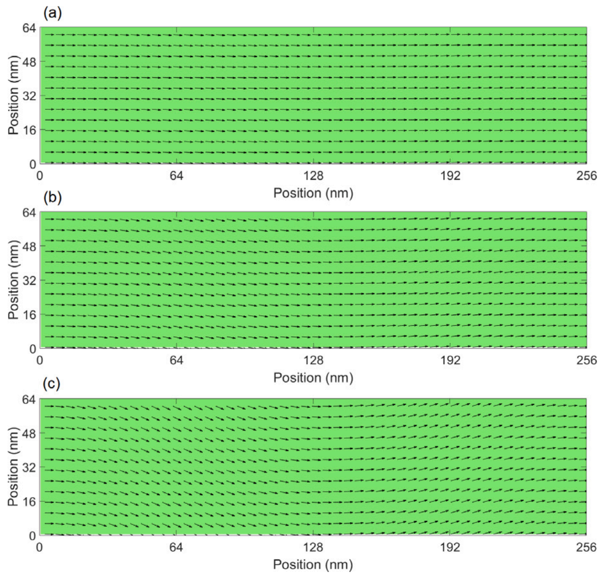

Fig. 11. Magnetization maps (limited to two periods) generated by a current-carrying coil with (a) $i_1 = 0.628$ mA, determining a magnetization fan angle $\Theta_F \approx 9°$; (b) $i_2 \approx 3.14$ mA, determining $\Theta_F \approx 25°$; (c) $i_3 = 62.8$ mA, determining $\Theta_F \approx 47°$.

Finally, the case with $d_c = 168$ nm but $B_0 = 0.04$ T, which *stretches* the resulting total field along x, so that $\Theta_F \approx 2.7°$. These values are just illustrative, being a systematic investigation outside the scope of the present paper, but we believe that they definitely help in understanding the *stretching effect* operated by either d_c or B_0.

Finally we use the Landau–Lifschitz–Gilbert equation (implemented in the Mumax3 solver) for the magnetization dynamics under the action of the above $\mathbf{B}_S$:

$$\frac{d\mathbf{M}}{dt} = \gamma \mathbf{M} \times \mathbf{B}_{eff} + \alpha \frac{\gamma}{M_s} \mathbf{M} \times (\mathbf{M} \times \mathbf{B}_{eff}), \tag{10}$$

where γ is the gyromagnetic ratio, α is the dimensionless damping term (we used the typical 0.01 for permalloy) and M_s is the saturation magnetization (we used 800 kA/m).

In the above equation, the effective field $\mathbf{B}_{eff} = \mathbf{B}_S + \mathbf{B}_{exch} + \mathbf{B}_{demag}$ is the sum of the applied, exchange, and demagnetizing fields, respectively, and $\mathbf{B}_S = \mathbf{B}_S(x, y)$ is the sinusoidal field distribution that we calculate at either a given i or d_c. We apply this field to the permalloy film subject of the investigation (see details in Section 2), which is prepared with an initially uniform magnetization oriented along x. The relaxed, equilibrium magnetization assumes a sinusoidal distribution, with its own specific undulation amplitude and fan angle which tend to those of the applied field only if B_S (i.e., the current intensity) is sufficiently large. Hence, differently from the vector field B_S, for the magnetization the current intensity is indeed an effective means to control its fan angle, and hence the magnon dynamics.

As an example, in Fig. 11 we show three magnetization maps obtained applying the field distribution of Fig. 10(a) with $i_1 = 0.628$ mA, $i_2 = 3.14$ mA and $i_3 = 62.8$ mA: the undulation amplitude is visibly increasing, and we quantified the magnetization fan angle to be, respectively, 9°, 25°, 47°. Note that the above values for i were chosen just to prove the principle of operation with visible changes in the magnetization maps.

In conclusion, a current carrying solenoid is an effective way to create a sinusoidal magnetization in a ferromagnetic film, and the current intensity a good parameter to control the magnetization undulation amplitude and hence the magnon dynamics.

Data availability

Data will be made available on request.

References

[1] G. Gubbiotti, Three-Dimensional Magnonics: Layered, Micro - and Nanostructures, Jenny Stanford Publishing, Singapore, 2019.

[2] A. Karenowska, A. Chumak, A. Serga, B. Hillebrands, Magnon spintronics, in: Handbook of Spintronics, 2014, pp. 1–38, http://dx.doi.org/10.1007/978-94-007-7604-3_53-1.

[3] Q. Wang, G. Csaba, R. Verba, A. Chumak, P. Pirro, Nanoscale magnonic networks, Phys. Rev. Appl. 21 (2024) 040503, https://link.aps.org/doi/10.1103/PhysRevApplied.21.040503.

[4] M. Kohda, T. Seki, Y. Yuminaka, T. Uemura, K. Kikuchi, G. Salis, Perspective on spin-based wave-parallel computing, Appl. Phys. Lett. 123 (2023) 190502, http://dx.doi.org/10.1063/5.0168083.

[5] A. Mahmoud, F. Ciubotaru, F. Vanderveken, A. Chumak, S. Hamdioui, C. Adelmann, S. Cotofana, Introduction to spin wave computing, J. Appl. Phys. 128 (2020) 161101, http://dx.doi.org/10.1063/5.0019328.

[6] G. Csaba, Á. Papp, W. Porod, Perspectives of using spin waves for computing and signal processing, Phys. Lett. A 381 (2017) 1471, http://dx.doi.org/10.1016/j.physleta.2017.02.042.

[7] P. Kolodin, B. Hillebrands, Spin-wave propagation across periodically corrugated thin metallic ferromagnetic films, J. Magn. Magn. Mater. 161 (1996) 199–202, https://www.sciencedirect.com/science/article/pii/S0304885396000194.

[8] H. Fuller, M. Hale, Determination of magnetization distribution in thin films using electron microscopy, J. Appl. Phys. 31 (1960) 238–248.

[9] K. Harte, Theory of magnetization ripple in ferromagnetic films, J. Appl. Phys. 39 (1968) 1503–1524.

[10] F. Montoncello, G. Gubbiotti, Controlling the three dimensional propagation of spin waves in continuous ferromagnetic films with an increasing out of plane undulation, Sci. Rep. 11 (2021) 21344, http://dx.doi.org/10.1038/s41598-021-00479-0.

[11] L. Giovannini, Theory of dipole-exchange spin-wave propagation in periodically corrugated films, Phys. Rev. B 105 (2022) 214426, https://link.aps.org/doi/10.1103/PhysRevB.105.214426.

[12] P. Graczyk, M. Krawczyk, S. Dhuey, W. Yang, H. Schmidt, G. Gubbiotti, Magnonic band gap and mode hybridization in continuous permalloy films induced by vertical dynamic coupling with an array of permalloy ellipses, Phys. Rev. B 98 (2018) 174420, https://link.aps.org/doi/10.1103/PhysRevB.98.174420.

[13] A. Frotanpour, J. Woods, B. Farmer, A. Kaphle, L. Long, L. Giovannini, F. Montoncello, Magnetization dynamics of a fibonacci-distorted kagome artificial spin ice, Phys. Rev. B 102 (2020) 224435.

[14] F. Montoncello, L. Giovannini, B. Farmer, L. De Long, Dynamic origin of segment magnetization reversal in thin-film Penrose tilings, J. Magn. Magn. Mater. 423 (2017) 158–163, http://dx.doi.org/10.1016/j.jmmm.2016.09.090.

[15] V.S. Bhat, J. Sklenar, B. Farmer, J. Woods, J.T. Hastings, S.J. Lee, J.B. Ketterson, L.E. De Long, Controlled magnetic reversal in permalloy films patterned into artificial quasicrystals, Phys. Rev. Lett. 111 (2013) 077201, http://dx.doi.org/10.1103/PhysRevLett.111.077201.

[16] B. Farmer, V. Bhat, J. Sklenar, E. Teipel, J. Ketterson, J. Hastings, L. De Long, Magnetic response of aperiodic wire networks based on Fibonacci distortions of square antidot lattices, J. Appl. Phys. 117 (2015) 17B714, http://dx.doi.org/10.1063/1.4913820.

[17] R. Sultana, M. Kaffash, G. Gubbiotti, Y. Ji, M. Jungfleisch, F. Montoncello, Magnon-Magnon interaction induced by dynamic coupling in a hybrid magnonic crystal, ACS Appl. Electron. Mater. 8 (2026) 482–492, http://dx.doi.org/10.1021/acsaelm.5c02128.

[18] P. Micaletti, F. Montoncello, Dynamic footprints of the specific artificial spin ice microstate on its spin waves, Magnetochemistry 9 (2023) https://www.mdpi.com/2312-7481/9/6/158.

[19] R. Negrello, F. Montoncello, M. Kaffash, M. Jungfleisch, G. Gubbiotti, Dynamic coupling and spin-wave dispersions in a magnetic hybrid system made of an artificial spin-ice structure and an extended NiFe underlayer, APL Mater. 10 (2022) 091115, http://dx.doi.org/10.1063/5.0102571.

[20] S. Ladak, A. Fernández-Pacheco, P. Fischer, Science and technology of 3D magnetic nanostructures, APL Mater. 10 (2022) 5, http://dx.doi.org/10.1063/5.0136801.

[21] F. Montoncello, M. Kaffash, H. Carfagno, M. Doty, G. Gubbiotti, M. Jungfleisch, A Brillouin light scattering study of the spin-wave magnetic field dependence in a magnetic hybrid system made of an artificial spin-ice structure and a film underlayer, J. Appl. Phys. 133 (2023) 083901, http://dx.doi.org/10.1063/5.0140866.

[22] T. Dion, K. Stenning, A. Vanstone, H. Holder, R. Sultana, G. Alatteili, V. Martinez, M. Kaffash, T. Kimura, R. Oulton, W. Branford, H. Kurebayashi, E. Iacocca, M. Jungfleisch, J. Gartside, Ultrastrong magnon-magnon coupling and chiral spin-texture control in a dipolar 3D multilayered artificial spin-vortex ice, Nat. Commun. 15 (2024) 4077, http://dx.doi.org/10.1038/s41467-024-48080-z.

[23] P. Micaletti, A. Roxburgh, E. Iacocca, M. Marzolla, F. Montoncello, Magnonic analog of a metal-to-insulator transition in a multiferroic heterostructure, J. Appl. Phys. 137 (2025) 153906, http://dx.doi.org/10.1063/5.0250690.

[24] H. Qin, R. Dreyer, G. Woltersdorf, T. Taniyama, S. van Dijken, Electric-field control of propagating spin waves by ferroelectric domain-wall motion in a multiferroic heterostructure, Adv. Mater. 33 (2021) 2100646, https://onlinelibrary.wiley.com/doi/abs/10.1002/adma.202100646.

[25] J. Kharlan, K. Szulc, J. Kłos, G. Centała, Tunable magnonic crystal in a hybrid superconductor–ferrimagnet nanostructure, Sci. Rep. 14 (2024) 25594, http://dx.doi.org/10.1038/s41598-024-75492-0.

[26] I. Golovchanskiy, N. Abramov, V. Stolyarov, V. Chichkov, M. Silaev, I. Shchetinin, A. Golubov, V. Ryazanov, A. Ustinov, M. Kupriyanov, Magnetization dynamics in proximity-coupled superconductor-ferromagnet-superconductor multilayers, Phys. Rev. Appl. 14 (2020) 024086, https://link.aps.org/doi/10.1103/PhysRevApplied.14.024086.

[27] I. Golovchanskiy, N. Abramov, V. Stolyarov, A. Golubov, V. Ryazanov, A. Ustinov, Nonlinear spin waves in ferromagnetic/superconductor hybrids, J. Appl. Phys. 127 (2020) 093903, http://dx.doi.org/10.1063/1.5141793.

[28] P. Micaletti, A. Roxburgh, E. Iacocca, M. Marzolla, F. Montoncello, A sinusoidal magnetization distribution as an original way to generate a versatile magnonic crystal for magnon propagation, J. Magn. Magn. Mater. 622 (2025) 172959, https://www.sciencedirect.com/science/article/pii/S0304885325001908.

[29] A. Chumak, T. Neumann, A. Serga, B. Hillebrands, M. Kostylev, A current-controlled, dynamic magnonic crystal, J. Phys. D: Appl. Phys. 42 (2009) 205005, http://dx.doi.org/10.1088/0022-3727/42/20/205005.

[30] A. Chumak, P. Kabos, M. Wu, C. Abert, C. Adelmann, A. Adeyeye, J. Åkerman, F. Aliev, A. Anane, A. Awad, C. Back, A. Barman, G. Bauer, M. Becherer, E. Beginin, V. Bittencourt, Y. Blanter, P. Bortolotti, I. Boventer, D. Bozhko, S. Bunyaev, J. Carmiggelt, R. Cheenikundil, F. Ciubotaru, S. Cotofana, G. Csaba, O. Dobrovolskiy, C. Dubs, M. Elyasi, K. Fripp, H. Fulara, I. Golovchanskiy, C. Gonzalez-Ballestero, P. Graczyk, D. Grundler, P. Gruszecki, G. Gubbiotti, K. Guslienko, A. Haldar, S. Hamdioui, R. Hertel, B. Hillebrands, T. Hioki, A. Houshang, C. Hu, H. Huebl, M. Huth, E. Iacocca, M. Jungfleisch, G. Kakazei, A. Khitun, R. Khymyn, T. Kikkawa, M. Kläui, O. Klein, J. Kłos, S. Knauer, S. Koraltan, M. Kostylev, M. Krawczyk, I. Krivorotov, V. Kruglyak, D. Lachance-Quirion, S. Ladak, R. Lebrun, Y. Li, M. Lindner, R. Macêdo, S. Mayr, G. Melkov, S. Mieszczak, Y. Nakamura, H. Nembach, A. Nikitin, S. Nikitov, V. Novosad, J. Otálora, Y. Otani, A. Papp, B. Pigeau, P. Pirro, W. Porod, F. Porrati, H. Qin, B. Rana, T. Reimann, F. Riente, O. Romero-Isart, A. Ross, A. Sadovnikov, A. Safin, E. Saitoh, G. Schmidt, H. Schultheiss, K. Schultheiss, A. Serga, S. Sharma, J. Shaw, D. Suess, O. Surzhenko, K. Szulc, T. Taniguchi, M. Urbánek, K. Usami, A. Ustinov, T. Sar, S. Dijken, V. Vasyuchka, R. Verba, S. Kusminskiy, Q. Wang, M. Weides, M. Weiler, S. Wintz, S. Wolski, X. Zhang, Advances in magnetics roadmap on spin-wave computing, IEEE Trans. Magn. 58 (2022) 1–72.

[31] B. Flebus, D. Grundler, B. Rana, Y. Otani, I. Barsukov, A. Barman, G. Gubbiotti, P. Landeros, J. Akerman, U. Ebels, P. Pirro, V. Demidov, K. Schultheiss, G. Csaba, Q. Wang, F. Ciubotaru, D. Nikonov, P. Che, R. Hertel, T. Ono, D. Afanasiev, J. Mentink, T. Rasing, B. Hillebrands, S. Kusminskiy, W. Zhang, C. Du, A. Finco, T. Sar, Y. Luo, Y. Shiota, J. Sklenar, T. Yu, J. Rao, The 2024 magnonics roadmap, J. Phys.: Condens. Matter. 36 (2024) 363501.

[32] V. Risinggård, I. Kulagina, J. Linder, Electric field control of magnon-induced magnetization dynamics in multiferroics, Sci. Rep. 6 (2016) 31800, http://dx.doi.org/10.1038/srep31800.

[33] H. Park, S. Zhang, P. Meisenheimer, M. Ramesh, S. Husain, I. Harris, J. Íñiguez González, Z. Yao, R. Ramesh, S. Kim, Magnon thermal conductivity in multiferroics with spin cycloids, 2025, https://arxiv.org/abs/2503.11135.

[34] I. Harris, S. Husain, P. Meisenheimer, M. Ramesh, H. Park, L. Caretta, D. Schlom, Z. Yao, L. Martin, J. Íñiguez González, S. Kim, R. Ramesh, Symmetry-based phenomenological model for magnon transport in a multiferroic, Phys. Rev. Lett. 134 (2025) 016703, https://link.aps.org/doi/10.1103/PhysRevLett.134.016703.

[35] S. Tacchi, F. Montoncello, M. Madami, G. Gubbiotti, G. Carlotti, L. Giovannini, R. Zivieri, F. Nizzoli, S. Jain, A. Adeyeye, N. Singh, Band diagram of spin waves in a two-dimensional magnonic crystal, Phys. Rev. Lett. 107 (2011) 127204, https://link.aps.org/doi/10.1103/PhysRevLett.107.127204.

[36] F. Montoncello, L. Giovannini, Bandwidth broadening and asymmetric softening of collective spin waves in magnonic crystals, Appl. Phys. Lett. 104 (2014) 242407, http://dx.doi.org/10.1063/1.4883878.

[37] A. De, C. Banerjee, A. Kumar Chaurasiya, R. Mandal, Y. Otani, R. Kumar Mitra, A. Barman, Anisotropic spin-wave dispersion in two-dimensional Ni80Fe20 diatomic nanodot array, J. Magn. Magn. Mater. 491 (2019) 165557, https://www.sciencedirect.com/science/article/pii/S0304885319319006.

[38] D. Kumar, J. Kłos, M. Krawczyk, A. Barman, Magnonic band structure, complete bandgap, and collective spin wave excitation in nanoscale two-dimensional magnonic crystals, J. Appl. Phys. 115 (2014) 043917, http://dx.doi.org/10.1063/1.4862911.

[39] V. Bessonov, M. Mruczkiewicz, R. Gieniusz, U. Guzowska, A. Maziewski, A. Stognij, M. Krawczyk, Magnonic band gaps in YIG-based one-dimensional magnonic crystals: An array of grooves versus an array of metallic stripes, Phys. Rev. B 91 (2015) 104421, https://link.aps.org/doi/10.1103/PhysRevB.91.104421.

[40] G. Gubbiotti, F. Montoncello, S. Tacchi, M. Madami, G. Carlotti, L. Giovannini, J. Ding, A. Adeyeye, Angle-resolved spin wave band diagrams of square antidot lattices studied by Brillouin light scattering, Appl. Phys. Lett. 106 (2015) 262406, http://dx.doi.org/10.1063/1.4923271.

[41] F. Ma, H. Lim, V. Zhang, S. Ng, M. Kuok, Magnonic band structure investigation of one-dimensional bi-component magnonic crystal waveguides, Nanoscale Res. Lett. 7 (2012) 498, http://dx.doi.org/10.1186/1556-276X-7-498.

[42] M. Krawczyk, S. Mamica, M. Mruczkiewicz, J. Klos, S. Tacchi, M. Madami, G. Gubbiotti, G. Duerr, D. Grundler, Magnonic band structures in two-dimensional bi-component magnonic crystals with in-plane magnetization, J. Phys. D: Appl. Phys. 46 (2013) 495003, http://dx.doi.org/10.1088/0022-3727/46/49/495003.

[43] P. Alvarado-Seguel, R. Gallardo, Band structure of a one-dimensional bilayer magnonic crystal, Phys. Rev. B 100 (2019) 144415, https://link.aps.org/doi/10.1103/PhysRevB.100.144415.

[44] N. Kuznetsov, H. Qin, L. Flajšman, S. Dijken, Dynamic magnonic crystals based on spatiotemporal plasmon excitation, Adv. Mater. 37 (2025) 2502474, https://advanced.onlinelibrary.wiley.com/doi/abs/10.1002/adma.202502474.

[45] A. Chumak, V. Tiberkevich, A. Karenowska, A. Serga, J. Gregg, A. Slavin, B. Hillebrands, All-linear time reversal by a dynamic artificial crystal, Nat. Commun. 1 (2010) 141, http://dx.doi.org/10.1038/ncomms1142.

[46] A. Vansteenkiste, J. Leliaert, M. Dvornik, M. Helsen, F. Garcia-Sanchez, B. Van Waeyenberge, The design and verification of MuMax3, AIP Adv. 4 (2014) 107133.

[47] H. Fangohr, G. Bordignon, M. Franchin, A. Knittel, P. Groot, T. Fischbacher, A new approach to (quasi) periodic boundary conditions in micromagnetics: The macrogeometry, J. Appl. Phys. 105 (2009) 07D529, http://dx.doi.org/10.1063/1.3068637.

[48] C. Kittel, On the theory of ferromagnetic resonance absorption, Phys. Rev. 73 (1948) 155.

[49] T. Lahtinen, K. Franke, S. Dijken, Electric-field control of magnetic domain wall motion and local magnetization reversal, Sci. Rep. 2 (2012) 258, http://dx.doi.org/10.1038/srep00258.

[50] T. Lahtinen, J. Tuomi, S. Dijken, Pattern transfer and electric-field-induced magnetic domain formation in multiferroic heterostructures, Adv. Mater. 23 (2011) 3187–3191, https://onlinelibrary.wiley.com/doi/abs/10.1002/adma.201100426.

[51] D. Kuźma, F. Montoncello, P. Sobieszczyk, A. Wal, L. Giovannini, P. Zieliński, Spin wave propagation properties across configurational antiferro/ferro-magnetic transitions, J. Appl. Phys. 124 (2018) 223902, http://dx.doi.org/10.1063/1.5057419.

[52] C. Wang, S. Cheng, W. Hsueh, High spin current density in gate-tunable spin-valves based on graphene nanoribbons, Sci. Rep. 13 (2023) 9234, http://dx.doi.org/10.1038/s41598-023-36478-6.

[53] Q. Guo, Z. Ren, H. Bai, X. Wang, G. Yu, W. He, J. Teng, T. Zhu, Current-induced magnetization switching in perpendicularly magnetized v/cofeb/mgo multilayers, Phys. Rev. B 104 (2021) 224429, https://link.aps.org/doi/10.1103/PhysRevB.104.224429.